



## Z-scheme system of $\text{WO}_3@\text{MoS}_2/\text{CdS}$ for photocatalytic evolution $\text{H}_2$ : $\text{MoS}_2$ as the charge transfer mode switcher, electron-hole mediator and cocatalyst

Lulu Zhang<sup>a</sup>, Hongwen Zhang<sup>a</sup>, Cankun Jiang<sup>a</sup>, Jie Yuan<sup>a</sup>, Xueyan Huang<sup>a</sup>, Ping Liu<sup>a,\*</sup>, Wenhui Feng<sup>b,\*</sup>

<sup>a</sup> Research Institute of Photocatalysis, State Key Laboratory of Photocatalysis on Energy and Environment, Fuzhou University, Fuzhou 350002, PR China

<sup>b</sup> Hunan Provincial Collaborative Innovation Center for Environment and Energy Photocatalysis, Changsha University, Changsha 410022, PR China



### ARTICLE INFO

#### Keywords:

Z-scheme  
Charge transfer mode switcher  
Electron-hole mediator  
Cocatalyst

### ABSTRACT

A novel ternary Z-scheme system of  $\text{WO}_3@\text{MoS}_2/\text{CdS}$  is successfully constructed using a three-step wet-chemical route, where  $\text{MoS}_2$  locates between the rod-shaped  $\text{WO}_3$  and  $\text{CdS}$  nanoparticles and simultaneously plays multiple roles of the charge transfer mode switcher, electron-hole mediator and cocatalyst. As a charge transfer mode switcher,  $\text{MoS}_2$  can transform the conventional type-II charge transfer mode to Z-scheme. In such a Z-scheme system, as an electron-hole mediator,  $\text{MoS}_2$  is applied to quench the energy of the electrons from  $\text{WO}_3$  and the holes from  $\text{CdS}$  in shorten length, and thus the more left electrons from  $\text{CdS}$  can transfer to  $\text{MoS}_2$ , which can be further applied to photocatalytic evolution  $\text{H}_2$  owing to the cocatalyst role of  $\text{MoS}_2$ . Benefiting from the multifunctional roles of  $\text{MoS}_2$ , such a Z-scheme system of  $\text{WO}_3@\text{MoS}_2/\text{CdS}$  shows an enhanced photocatalytic performance.

### 1. Introduction

Semiconductor driven photocatalysis has long been emerged as an attractive protocol to environmental pollution and energy crisis [1–5]. To date, many efforts have been made to enhance the photocatalytic efficiency, and among them, construction of type-II heterostructure can be seen as a potential strategy due to its extended light absorption range and decreased recombination of charge carriers compared with individuals [6,7]. Usually, this kind of heterostructure contains two charge carrier transfer modes of conventional type-II and Z-scheme [8]. As is known, the efficient charge separation of conventional type-II is at the cost of its redox ability [9–11]. Therefore, in order to achieve the excellent performance and wide application prospect, compared with conventional type-II, Z-scheme mode, which simultaneously possesses the high charge separation efficiency and strong redox property, is more potential and suitable [12–17]. Thus, many researches are focused on directly conducting a Z-scheme system [18,19]. Nevertheless, how to switch the charge transfer mode from conventional type-II to favor Z-scheme is more challenging and extensive.

Besides, in a Z-scheme system, enhancing the transfer rate of electron on the interface of PS I (photosystem I, where the photogenerated holes with a lower oxidation ability) and PS II (photosystem II, where the photogenerated electrons with a lower reduction ability) is very

urgent. Up to now, many shuttle redox mediators have been applied to accelerate the electrons transfer. Unfortunately, there are also some limitations. For reversible redox mediators, backward reactions are easily happened, and its application is only constrained in liquid phase reactions [16,20]. For solid electron mediator, the noble metals (Au, Ag and so on) and graphene are usually explored. In addition to the high cost, all of them only can transfer electrons rather than both of electrons and holes [21–25]. In this case, only the electrons from PS II can transfer to PS I, leading to too long transmission distances, which provides opportunity for charges recombination on the interface. Therefore, if introducing an electron-hole mediator into Z-scheme system, which not only transfer electrons, but the holes, the electrons from PS II will be recombined with the holes from PS I in this mediator, which just like “iceberg” for quenching the energy of these charge carriers. Thus, the transmission distances can be greatly shortened, which can contribute to promote the favor separation and transfer of charge carriers, leading to the enhanced performance.

Thus, in a Z-scheme system contained electron-hole mediator, more electrons from PS I and holes from PS II are left to participate in photocatalytic reaction. Nevertheless, if these charge carriers can't be consumed in time, the recombination will happen again on the surface. Therefore, in order to further accelerate surface separation of carriers and improve the efficiency of photocatalyst systems, cocatalyst loading,

\* Corresponding author.

E-mail addresses: [liuping@fzu.edu.cn](mailto:liuping@fzu.edu.cn) (P. Liu), [fengwenhui1991@126.com](mailto:fengwenhui1991@126.com) (W. Feng).

as an effective way, has been widely studied [26,27]. The main roles of such cocatalyst are to collect photogenerated charge carriers and host active sites for surface chemical reactions by the carriers [28–31]. However, extra introducing cocatalyst into Z-scheme system may increase the cost of materials. Therefore, if a potential candidate can simultaneously play multiple roles such as switching the charge transfer mode, electron-hole mediator and cocatalyst, the performance of Z-scheme system will be improved significantly.

Herein, a novel model structure  $\text{WO}_3@\text{MoS}_2/\text{CdS}$ , where the  $\text{MoS}_2$  locates at  $\text{WO}_3/\text{CdS}$  interface, is successfully constructed using a three-step wet-chemical route. As a charge transfer mode switcher,  $\text{MoS}_2$  can transform the conventional type-II charge transfer mode to Z-scheme. As an electron-hole mediator,  $\text{MoS}_2$  can both transfer electrons and holes, where  $\text{MoS}_2$  just like an “iceberg” to quench the energy of the electrons from  $\text{WO}_3$  and the holes from  $\text{CdS}$  in shorten length. As a cocatalyst, the CB of  $\text{MoS}_2$  can provide active sites for photocatalytic evolution  $\text{H}_2$  driven by the electrons from  $\text{CdS}$ . Since  $\text{MoS}_2$  simultaneous acts as the mentioned functions, the  $\text{WO}_3@\text{MoS}_2/\text{CdS}$  can be shown an improved photocatalytic performance compared with  $\text{WO}_3/\text{CdS}$  or  $\text{MoS}_2/\text{CdS}$ .

## 2. Experimental procedures

### 2.1. Materials

Sodium tungstate ( $\text{Na}_2\text{WO}_4 \cdot 2\text{H}_2\text{O}$ ), sodium chloride ( $\text{NaCl}$ ), concentrated hydrochloric acid (HCl), absolute ethanol, glucose solution, sodium molybdate ( $\text{Na}_2\text{MoO}_4 \cdot 2\text{H}_2\text{O}$ ), thiourea ( $\text{CH}_4\text{N}_2\text{S}$ ),  $\text{Cd}(\text{CH}_3\text{COO})_2$  were purchased from Sinopharm Chemical Reagent Co., Ltd. (Shanghai, China). The above chemical reagents were of analytical grade and without further purification. Deionized (DI) water was used throughout this work.

### 2.2. Synthesis of photocatalysts

#### 2.2.1. Preparation of $\text{WO}_3$

The  $\text{WO}_3$  was prepared according to previous literatures [32]. In a typical synthesis, 1 g of  $\text{Na}_2\text{WO}_4 \cdot 2\text{H}_2\text{O}$  and 0.5 g of  $\text{NaCl}$  were dissolved in 20 mL of water. The pH of the solution was adjusted to 2 by 4 M HCl. The above solution was stirred for 60 min and then transferred into a Teflon-lined stainless steel autoclave (50 mL) and heated at 180 °C for 24 h. After cooled down to room temperature, the sample was centrifugalized with distilled water and absolute ethanol several times and dried in a 60 °C oven.

#### 2.2.2. Preparation of $\text{WO}_3@\text{MoS}_2$

$\text{WO}_3@\text{MoS}_2$  was prepared through the following process [33,34]. 0.1 g  $\text{WO}_3$  was added to 30 mL of glucose solution (0.5 M) and ultrasound 20 min. Then 0.5 g of  $\text{Na}_2\text{MoO}_4 \cdot 2\text{H}_2\text{O}$  and 1 g of  $\text{CH}_4\text{N}_2\text{S}$  were added and stirring for 30 min. The mixed solution was then transferred to a 50 mL Teflon-lined stainless steel autoclave and heated at 200 °C for 12 h. Finally, the as-obtained sample was centrifugalized with distilled water and absolute ethanol several times.

#### 2.2.3. Preparation of $\text{WO}_3@\text{MoS}_2/\text{CdS}$

$\text{WO}_3@\text{MoS}_2/\text{CdS}$  was fabricated by chemical bath deposition according to literature [15]. Typically, 50 mg of  $\text{WO}_3@\text{MoS}_2$  sample was added in 60 mL de-ionized water containing 1 g  $\text{Cd}(\text{CH}_3\text{COO})_2 \cdot 2\text{H}_2\text{O}$ . Subsequently, the above suspension was stirred for 30 min in dark. 0.6 g  $\text{CH}_4\text{N}_2\text{S}$  was then added to the suspension. After the chemical bath deposition at 80 °C for 20 min, the precipitate was collected by centrifugation and washed with de-ionized water several times.

#### 2.2.4. Preparation of $\text{WO}_3/\text{CdS}$

$\text{WO}_3/\text{CdS}$  was synthesized by the method similar to  $\text{WO}_3@\text{MoS}_2/\text{CdS}$  but adding  $\text{WO}_3$  instead of  $\text{WO}_3@\text{MoS}_2$ .

#### 2.2.5. Preparation of $\text{MoS}_2/\text{CdS}$

$\text{MoS}_2/\text{CdS}$  was synthesized by the method similar to  $\text{WO}_3@\text{MoS}_2/\text{CdS}$  but adding  $\text{MoS}_2$  instead of  $\text{WO}_3@\text{MoS}_2$ .

For comparison, the pure  $\text{MoS}_2$  and  $\text{CdS}$  were synthesized under the same experimental conditions, respectively.

#### 2.2.6. Preparation of $\text{CdS}$

$\text{CdS}$  was synthesized by the method similar to  $\text{WO}_3/\text{CdS}$  but without adding  $\text{WO}_3$ .

#### 2.2.7. Preparation of $\text{MoS}_2$

$\text{MoS}_2$  was synthesized by the method similar to  $\text{WO}_3@\text{MoS}_2$  but without adding  $\text{WO}_3$ .

## 2.3. Characterization

The crystal structure of as-prepared samples were carried out by a Bruker D8 ADVANCE X-ray diffraction with Cu K $\alpha$  radiation ( $\lambda = 0.15418 \text{ nm}$ ), which operated at 40 kV and 40 mA. The morphologies were obtained with a HITACHI SU8000 field-emission scanning electron microscope (SEM) and a transmission electron microscope (TEM) and high-resolution transmission electron micrographs (HRTEM, FEI Tecnai G20) with an accelerating voltage of 200 kV. X-ray photoelectron spectra (XPS) was characterized by a Thermo Scientific ESCA Lab 250 system, with a monochromatic Al K $\alpha$  as the X-ray source, hemispherical analyzer. The UV-Vis diffuse reflectance spectra (DRS) of samples were measured by a Carry 5000 UV-vis spectrophotometer, where  $\text{BaSO}_4$  was served as the background. Photoluminescence spectrum was obtained using a Horiba Jobin-Yvon Fluorolog-3 spectrofluorometer with a 425 nm excitation wavelength.

## 2.4. Photoelectrochemical measurements

The photoelectrochemical properties of the samples were measured in a conventional three-electrode electrochemical workstation (CHI 660E, CH Instruments, Inc., Shanghai) with Ag/AgCl electrode as the reference electrode and Pt wire as the counter electrode. 0.2 M of aqueous  $\text{Na}_2\text{SO}_4$  solution was used as the supporting electrolyte. The sample electrode was prepared according to the following process: 50 mg sample was suspended in 0.5 mL of  $\text{C}_2\text{H}_5\text{OH}$ , which was used for spreading the sample onto the Fluorinedoped Tin Oxide (FTO) glass of 0.5 × 0.5 cm. The sample electrode was irradiated by a 300 W Xe arc lamp. Electrochemical impedance spectroscopy (EIS) under AC polarization (10 mV) was measured on another Potentiostat (ZAHNER).

## 2.5. Photocatalytic activity measurements

The photocatalytic activities of samples were evaluated by photocatalytic  $\text{H}_2$  evolution reaction. Typically, 30 mg photocatalyst was suspended in 100 mL mixed aqueous solution containing 10 vol.% of lactic acid, and then performed in a relatively vacuum system allocated an external glass reaction cell by the Labsolar-6A photocatalytic water decomposition hydrogen production system (Perfect light Technology Co. Ltd.). The suspension was degassed for 30 min to remove all air in solution and headspace. Then the vessel was vertically irradiated by a 300 W Xe lamp. The temperature of reaction solution was maintained at 5 °C. The amount of generated  $\text{H}_2$  was analyzed by a Techcomp GC7900 gas chromatograph with a thermal conductivity detector (TCD, molecular sieve 5A, argon carrier gas 99.999%).

## 3. Results and discussion

### 3.1. Structural properties of photocatalysts

The crystal structure and phase purity of as-synthesized materials are characterized by X-ray diffraction (XRD) analysis. As shown in

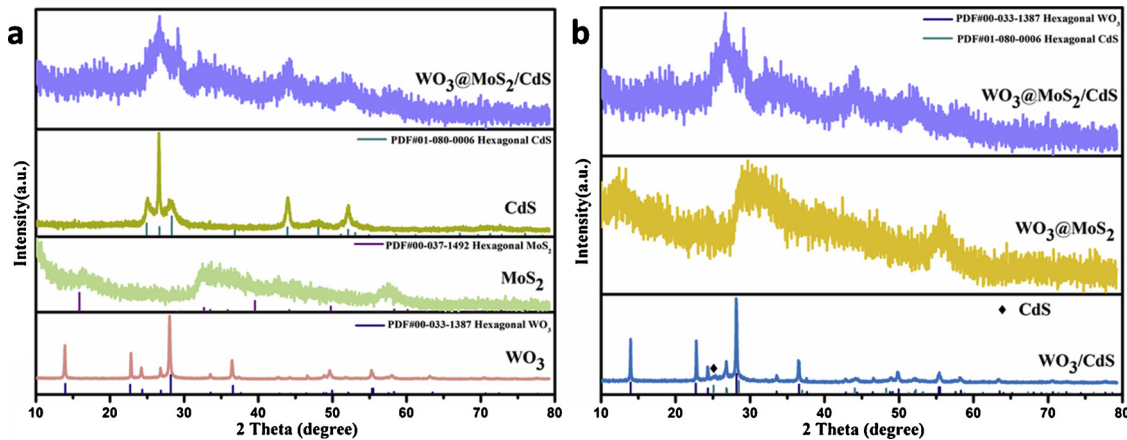


Fig. 1. XRD patterns of all samples.

Fig. 1a, the sharp peak patterns of  $\text{WO}_3$ ,  $\text{MoS}_2$  and  $\text{CdS}$  are well matched with the standard Joint Committee on Powder Diffraction Standards (JCPDS) card No. 00-033-1387, No. 00-037-1492 and No. 01-080-0006, which is assigned to hexagonal  $\text{WO}_3$ , hexagonal  $\text{MoS}_2$  and hexagonal  $\text{CdS}$ , respectively. As shown in Fig. 1b, it can be seen that the diffraction peak of  $\text{CdS}$  are more clearly shown at about  $25.02^\circ$  in the XRD pattern of  $\text{WO}_3/\text{CdS}$ . And combining with the SEM images of  $\text{WO}_3$  and  $\text{WO}_3/\text{CdS}$  shown in Fig. S1, it can be clearly seen that  $\text{CdS}$  nanoparticles are deposited onto the surface of  $\text{WO}_3$ , indicating that  $\text{CdS}$  is successfully deposited onto the  $\text{WO}_3$ . Besides, since only the diffraction peaks of  $\text{CdS}$  and  $\text{MoS}_2$  appear on the XRD pattern of the  $\text{WO}_3@\text{MoS}_2/\text{CdS}$ , and considering the preparation sequence of samples, it is considered that  $\text{MoS}_2$  may wrap on the surface of  $\text{WO}_3$ , and  $\text{CdS}$  may be deposited on  $\text{MoS}_2$  [7,34]. Thus,  $\text{MoS}_2$  may locate between  $\text{WO}_3$  and  $\text{CdS}$ . This hypothetical model also needs to be further confirmed by subsequent SEM and TEM characterizations.

SEM and TEM characterizations are further applied to obtain morphological and positional information of as-prepared samples. As displayed in Fig. 2a, pure  $\text{WO}_3$  shows rod-like structure with a diameter of 150 nm and a length of 1–2  $\mu\text{m}$  and relatively smooth surface. In Fig. 2b,  $\text{MoS}_2$  nanosheets are grown on the surface of the  $\text{WO}_3$  rods uniformly, and  $\text{WO}_3$  is encapsulated by  $\text{MoS}_2$ . As shown in Fig. 2c, the

smooth  $\text{MoS}_2$  nanosheets surfaces are roughened with the  $\text{CdS}$  uniformly grown on the surface of  $\text{MoS}_2$ . TEM investigation is applied to further confirm the crystal structures and morphologies of  $\text{WO}_3@\text{MoS}_2/\text{CdS}$ . As shown in Fig. 2e and f, the lattice fringe of  $\text{CdS}$  displays spacing of 0.355 nm, which matches well with the (100) plane of the hexagonal  $\text{CdS}$ . Fig. 2f shows a relatively blurry characteristic spacing of 0.316 nm, corresponding to the (200) lattice plane of hexagonal  $\text{WO}_3$ . The relatively blurry lattice fringe of  $\text{WO}_3$  may be attributed to the encapsulation by  $\text{MoS}_2$ . Besides, Fig. 2d shows the  $\text{WO}_3$  and  $\text{CdS}$  are isolated by  $\text{MoS}_2$ , which is consistent with the mentioned results of XRD and SEM.

### 3.2. Photocatalytic activity and stability

To date, we have successfully proved the composition and structure of  $\text{WO}_3@\text{MoS}_2/\text{CdS}$ . Then the photocatalytic  $\text{H}_2$  evolution performances of aforementioned composites are evaluated shown in Fig. 3. The activity of  $\text{WO}_3$  is hardly detectable owing to its too positive CB potential. And  $\text{WO}_3@\text{MoS}_2$  is almost inactive due to rapid recombination of photoinduced charge carriers of  $\text{MoS}_2$ . Besides, pure  $\text{CdS}$  shows very low activity ( $0.02 \text{ mmol h}^{-1} \text{ g}^{-1}$ ) because of rapid recombination of charge carriers.  $\text{WO}_3/\text{CdS}$  shows relatively low activity ( $0.21 \text{ mmol h}^{-1} \text{ g}^{-1}$ )

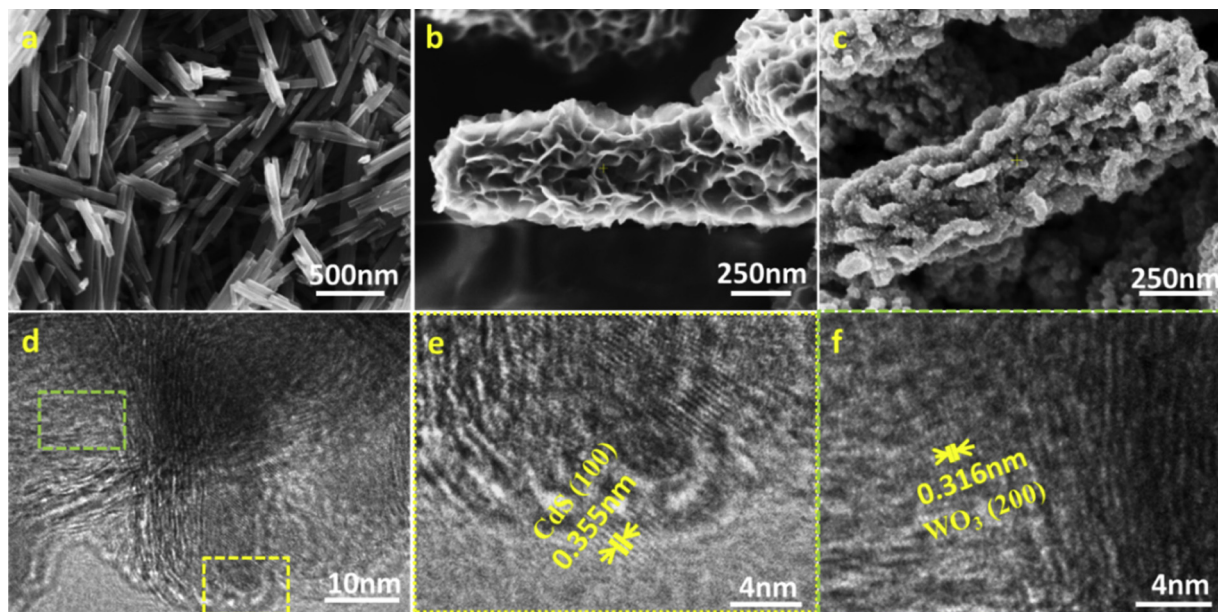


Fig. 2. Typical SEM images of  $\text{WO}_3$  (a),  $\text{WO}_3@\text{MoS}_2$  (b),  $\text{WO}_3@\text{MoS}_2/\text{CdS}$  (c), TEM image of  $\text{WO}_3@\text{MoS}_2/\text{CdS}$  (d) and HRTEM images (e) and (f) (For interpretation of the references to colour in this figure legend, the reader is referred to the web version of this article).

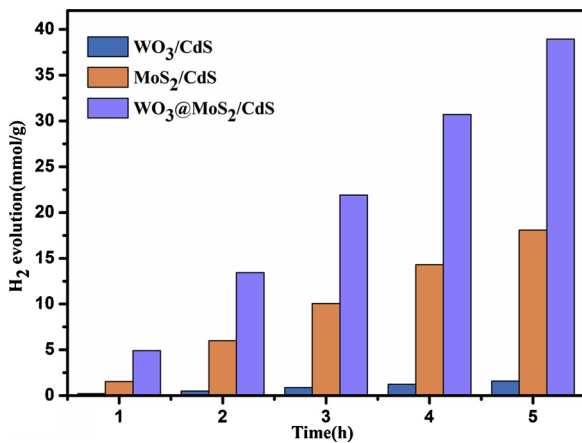


Fig. 3. Photocatalytic H<sub>2</sub> evolution rates of composites.

$h^{-1} g^{-1}$ ), which might be attributed to its charge transfer of conventional type-II. The corresponding evidences can be given by XPS data. The activity of MoS<sub>2</sub>/CdS is relatively high (3.6 mmol  $h^{-1} g^{-1}$ ) owing to the cocatalyst role of MoS<sub>2</sub>, which can enhance the charge separation and provide active site for photocatalytic evolution H<sub>2</sub>. Obviously, WO<sub>3</sub>@MoS<sub>2</sub>/CdS composite presents the maximum H<sub>2</sub> evolution (8.2 mmol  $h^{-1} g^{-1}$ ) than WO<sub>3</sub>/CdS or MoS<sub>2</sub>/CdS. The enhanced performance is usually attributed to the decreasing recombination of photogenerated electron-hole pairs and increasing numbers of favor charge carriers, which may be caused by MoS<sub>2</sub>. Therefore, the following part is to demonstrate the multifunctional roles of MoS<sub>2</sub>, which not only switches the charge transfer mode from type-II to Z-scheme, but acts as electron-hole mediator to shorten interface transmission distance and cocatalyst for providing active sites. Besides, as shown in Fig. S2, the novel Z-scheme system of WO<sub>3</sub>@MoS<sub>2</sub>/CdS present a satisfying stable performance for hydrogen production during a 12 h cycling test without refreshing the catalysts and sacrificial agents.

In order to demonstrate the roles of MoS<sub>2</sub> in enhancing performance of WO<sub>3</sub>@MoS<sub>2</sub>/CdS, XPS investigation can be seen as powerful evidence. After WO<sub>3</sub>@MoS<sub>2</sub>/CdS and WO<sub>3</sub>/CdS are undergone the same photocatalysis process, the two samples are referred to WO<sub>3</sub>@MoS<sub>2</sub>/CdS-used and WO<sub>3</sub>/CdS-used, respectively. As displayed in Fig. 4, the W 4f XPS spectra of pure WO<sub>3</sub> shows two dominant peaks, which are corresponded to W<sup>6+</sup> ions. While there are four peaks in WO<sub>3</sub>/CdS-used, the peaks at 37.7 and 35.6 eV are corresponded to W<sup>6+</sup> ions, and the dominant peaks at 36.3 and 34.1 eV are corresponded to W<sup>5+</sup> ions. This result of multiple valence states of W demonstrates the electrons

from CdS do transfer to WO<sub>3</sub>, and the charge transfer manner of WO<sub>3</sub>/CdS is traditional type-II [8,32]. In the W 4f XPS spectra of WO<sub>3</sub>@MoS<sub>2</sub>/CdS-used, there are two dominant peaks, which are corresponded to W<sup>6+</sup> ions, indicating that there may be no electrons transfer to WO<sub>3</sub>, and the charge transfer mode of WO<sub>3</sub>@MoS<sub>2</sub>/CdS may follow Z-scheme. These results also can further demonstrate that MoS<sub>2</sub> is vertically located on the WO<sub>3</sub> without horizontal coating. In this case, WO<sub>3</sub> can be excited by light to produce photogenerated charge carriers. Besides, owing to electron migration can cause a shift in the binding energy of a specific element, the charge transfer also can be further proved by XPS patterns. According to Fig. 4, a respective negative shift of W 4f state in the binding energy of WO<sub>3</sub>/CdS-used compared with WO<sub>3</sub> can be clearly observed, indicating the photogenerated electrons are moved from CdS to WO<sub>3</sub>, which is accordance with the result of multiple valence states of W. While in WO<sub>3</sub>@MoS<sub>2</sub>/CdS-used, the way of electron transfer is inversed: W 4f binding energy is shifted in positive direction compared with WO<sub>3</sub>, which reveals the electrons from WO<sub>3</sub> are transferred to MoS<sub>2</sub>. According to the aforementioned analyzes, it can be concluded that MoS<sub>2</sub> can be as a charge transfer mode switcher for transforming the conventional type-II to Z-scheme.

In order to further investigate the effect of MoS<sub>2</sub> on the interfacial charge transfer properties, electrochemical impedance spectroscopy (EIS) and transient photocurrent responses of as-synthesized materials are implemented. As shown in Fig. 5a and b, it is found that WO<sub>3</sub>@MoS<sub>2</sub>/CdS has a smallest radius of the semi-cycle arc in the Nyquist plot compared with that of other samples, which signifies that a more efficient interfacial charge transfer of WO<sub>3</sub>@MoS<sub>2</sub>/CdS on the electrode/electrolyte interface. As shown in Fig. 5c and d, it is worth noting that WO<sub>3</sub>@MoS<sub>2</sub>/CdS shows significantly enhanced photocurrent densities, which means that more effective charge separation and transmission is realized. These results further confirm that introducing MoS<sub>2</sub> into WO<sub>3</sub>/CdS can facilitate the surficial charge transfer and lead to an effective separation of photogenerated charge carriers, which induced a prominent increment of performance in the photocatalytic hydrogen process.

To further investigate the transfer and separation efficiency of the charge carriers, the photoluminescence (PL) spectra is employed and shown in Fig. S3. CdS displays a strong emission peak located at 580 nm, and WO<sub>3</sub>/CdS and MoS<sub>2</sub>/CdS both exhibit a relatively weak intensity. Moreover, WO<sub>3</sub>@MoS<sub>2</sub>/CdS shows a weaker PL intensity even than MoS<sub>2</sub>/CdS, demonstrating that the novel Z-scheme system can further inhibit the photogenerated carrier recombination of CdS. As a consequence, these results are in accordance with the XPS, EIS and transient photocurrent responses data analysis above, which confirm the multifunctional roles of MoS<sub>2</sub> in enhancing performance of WO<sub>3</sub>@MoS<sub>2</sub>/CdS.

Besides, the photocatalytic performance is also related to the photo-response characteristics of the photocatalyst. Thus, the optical absorption region needs to be confirmed and discussed in detail below. The optical properties of the as-prepared samples are investigated via UV-vis diffuse reflectance spectroscopy (DRS) shown in Fig. 6. Bare WO<sub>3</sub> shows a narrow absorption, and CdS exhibits a relatively wide absorption. Obviously, MoS<sub>2</sub> has a wide absorption in the visible-light region. According to Fig. 6b, WO<sub>3</sub>/CdS shows a weaker absorption compared with the other three samples. Notably, WO<sub>3</sub>@MoS<sub>2</sub>/CdS exhibits a wider absorption than MoS<sub>2</sub>/CdS, which means more photogenerated charge carriers can participate in photocatalytic reaction. Besides, the photocatalytic activities of WO<sub>3</sub>@MoS<sub>2</sub>/CdS and MoS<sub>2</sub>/CdS are compared under light irradiation of single wavelength at 475 nm to sure WO<sub>3</sub> can't be excited. In this case, this activity of both can reflect the effect of existential state of MoS<sub>2</sub> on photocatalytic performance. As shown in Fig. S4, MoS<sub>2</sub>/CdS shows higher performance compared with WO<sub>3</sub>@MoS<sub>2</sub>/CdS, which mainly due to the less mass of MoS<sub>2</sub>/CdS in WO<sub>3</sub>@MoS<sub>2</sub>/CdS than that in MoS<sub>2</sub>/CdS. Therefore, this result shows the importance of WO<sub>3</sub>, and further confirms the electron-hole mediator role of MoS<sub>2</sub> is one of the main reasons to enhance photocatalytic performance.

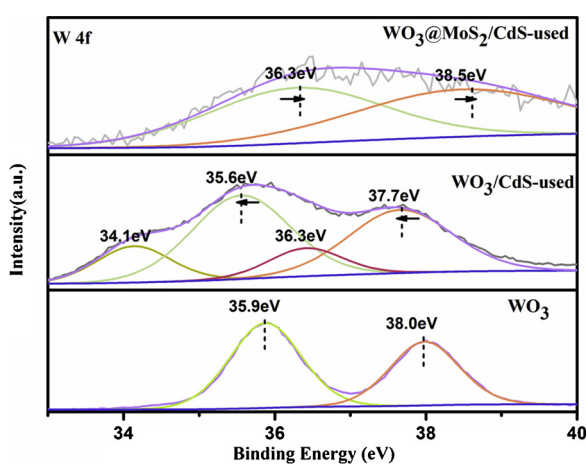


Fig. 4. (a) W 4f XPS spectra of WO<sub>3</sub>, WO<sub>3</sub>/CdS-used and WO<sub>3</sub>@MoS<sub>2</sub>/CdS-used.

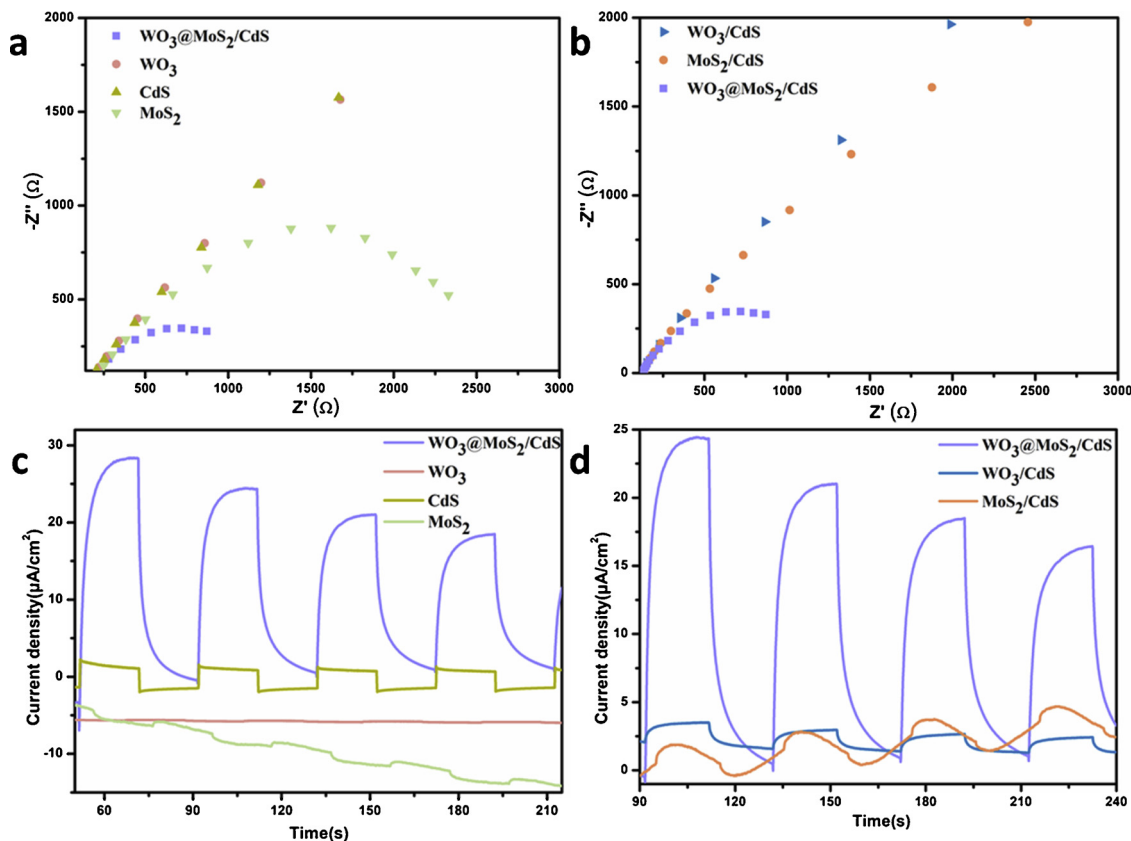


Fig. 5. photo-electrochemical impedance spectra (a) and transient photocurrent responses (b) of all samples.

### 3.3. Photocatalytic mechanism

Before proposing the mechanism for the photocatalytic  $\text{H}_2$  production, the energy level structure of  $\text{WO}_3$ ,  $\text{MoS}_2$  and  $\text{CdS}$  should be ascertained. According to Fig. S5, the  $E_g$  of  $\text{WO}_3$  and  $\text{CdS}$  are 2.86 and 2.23 eV, respectively. As Fig. S6 shown, the VB of  $\text{WO}_3$  and  $\text{CdS}$  are 3.18 and 1.86 V respectively, which are measured by XPS data. According to  $E_{\text{CB}} = E_{\text{VB}} - E_g$ , the CB of  $\text{WO}_3$  and  $\text{CdS}$  are 0.32 and  $-0.37$  eV, respectively. Owing to strong light absorption of  $\text{MoS}_2$ , it's difficult to measure the  $E_g$  of  $\text{MoS}_2$ . Therefore, by referencing to corresponding literatures [34], the CB and VB of  $\text{MoS}_2$  are  $-0.14$  and 1.78 eV, respectively. Based on the above test results, the CB and VB positions of the three semiconductors are drawn in Fig. 7.

On the basis of the mentioned results, the mechanism for the photocatalytic  $\text{H}_2$  production by  $\text{WO}_3@\text{MoS}_2/\text{CdS}$  can be clearly proposed.

As depicted in Fig. 7, both  $\text{WO}_3$  and  $\text{CdS}$  can simultaneously be excited and generate electron-hole pairs. The photo-induced electrons on the CB of  $\text{WO}_3$  and holes from VB of  $\text{CdS}$  both can be transferred to  $\text{MoS}_2$  ("iceberg") and then recombined. In this case, the transmission distances can be shortened significantly, leading to promote the favor separation and transfer of charge carriers, and the whole transfer mode of charge carriers follows Z-scheme mechanism. In this case, the more electrons on the CB of  $\text{CdS}$  can be moved to  $\text{MoS}_2$ , which provides active sites for the photocatalytic process, leading to high performance of  $\text{H}_2$  production.

### 4. Conclusions

In summary, a novel model structure  $\text{WO}_3@\text{MoS}_2/\text{CdS}$ , where the  $\text{MoS}_2$  locates at the interface of  $\text{WO}_3/\text{CdS}$ , is successfully constructed

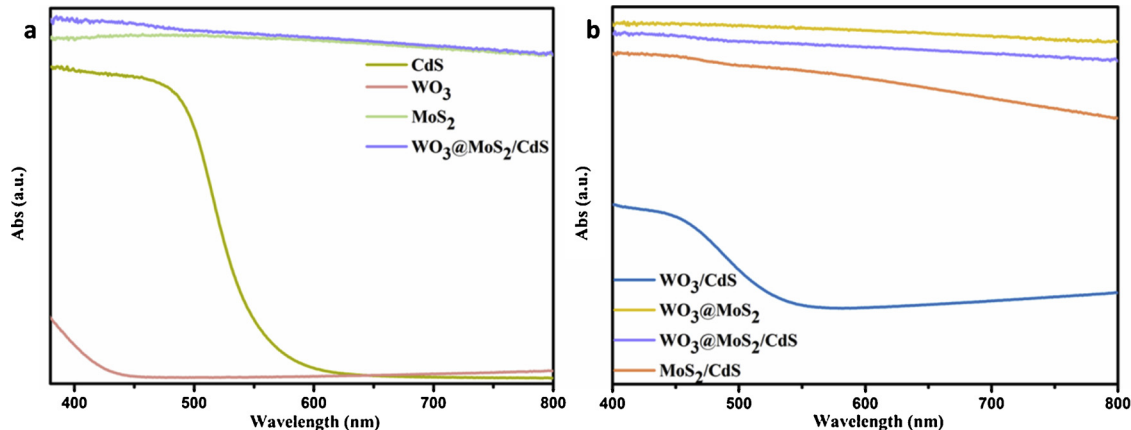


Fig. 6. (a) UV-vis diffuse reflectance spectrum of samples.

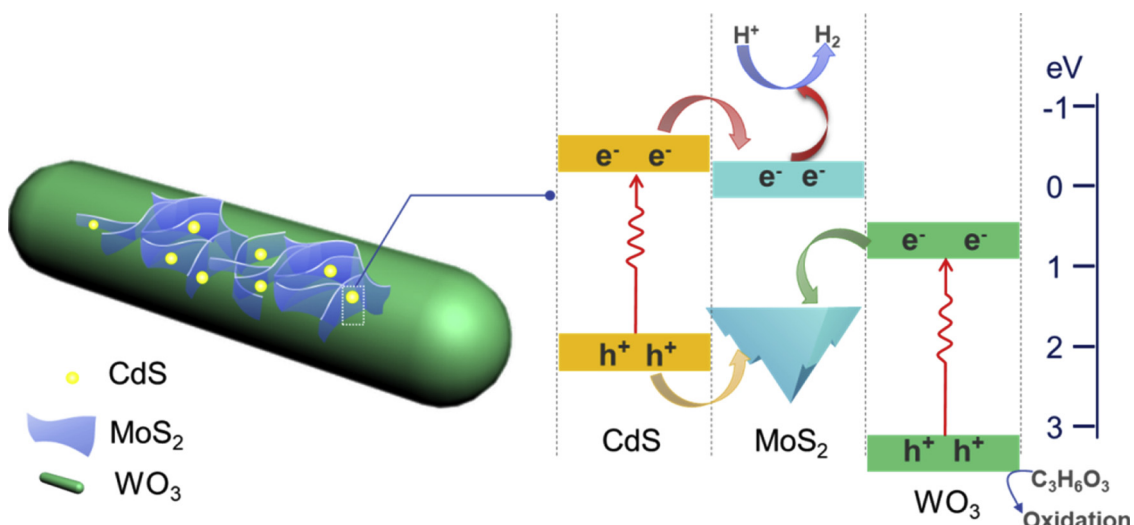


Fig. 7. Proposed mechanisms of  $\text{WO}_3@\text{MoS}_2/\text{CdS}$  for photocatalytic  $\text{H}_2$  evolution.

using a three-step wet-chemical route. There are three function roles of  $\text{MoS}_2$  in  $\text{WO}_3@\text{MoS}_2/\text{CdS}$ : charge carriers transfer switcher, electron-hole mediator and co-catalyst. Such established  $\text{WO}_3@\text{MoS}_2/\text{CdS}$  offers a new strategy for the development of effective Z-scheme systems, which further improve the photocatalytic performance.

#### Declaration of Competing Interest

The authors declare that they have no known competing financial interests or personal relationships that could have appeared to influence the work reported in this paper.

#### Acknowledgements

This work is supported by the National Natural Science Foundation of China (21673041, 21802007) and Science & Technology Plan Project of Changsha (kc1809020).

#### Appendix A. Supplementary data

Supplementary material related to this article can be found, in the online version, at doi:<https://doi.org/10.1016/j.apcatb.2019.118073>.

#### References

- [1] S. Chen, Y. Qi, T. Hisatomi, Q. Ding, T. Asai, Z. Li, S.S. Ma, F. Zhang, K. Domen, C. Li, *Angew. Chemie* 54 (2015) 8498–8501.
- [2] Y. Wang, Z. Zhang, L. Zhang, Z. Luo, J. Shen, H. Lin, J. Long, J.C.S. Wu, X. Fu, X. Wang, C. Li, J. Am. Chem. Soc. 140 (2018) 14595–14598.
- [3] Z. He, J. Fu, B. Cheng, J. Yu, S. Cao, *Appl. Catal. B Environ.* 205 (2017) 104–111.
- [4] Z. Lou, M. Zhu, X. Yang, Y. Zhang, M.-H. Whangbo, B. Li, B. Huang, *Appl. Catal. B Environ.* 226 (2018) 10–15.
- [5] Y.-J. Yuan, D.-Q. Chen, M. Xiong, J.-S. Zhong, Z.-Y. Wan, Y. Zhou, S. Liu, Z.-T. Yu, L.-X. Yang, Z.-G. Zou, *Appl. Catal. B Environ.* 204 (2017) 58–66.
- [6] M. Zhou, S. Wang, P. Yang, C. Huang, X. Wang, *ACS Catal.* (2018) 4928–4936.
- [7] B. Sun, W. Zhou, H. Li, L. Ren, P. Qiao, W. Li, H. Fu, *Adv. Mater.* 30 (2018) e1804282.
- [8] L. Zhang, H. Zhang, B. Wang, X. Huang, Y. Ye, R. Lei, W. Feng, P. Liu, *Appl. Catal. B* 244 (2019) 529–535.
- [9] B. Xu, P. He, H. Liu, P. Wang, G. Zhou, X. Wang, *Angew. Chemie* 53 (2014) 2339–2343.
- [10] L. Jinhai, M. Han, Y. Guo, F. Wang, L. Meng, D. Mao, S. Ding, C. Sun, *Appl. Catal. A Gen.* 524 (2016) 105–114.
- [11] H. Zhang, L. Ma, J. Ming, B. Liu, Y. Zhao, Y. Hou, Z. Ding, C. Xu, Z. Zhang, J. Long, *Appl. Catal. B Environ.* 243 (2019) 481–489.
- [12] J. Low, B. Dai, T. Tong, C. Jiang, J. Yu, *Adv. Mater.* 31 (2019) e1802981.
- [13] Y. Chao, P. Zhou, N. Li, J. Lai, Y. Yang, Y. Zhang, Y. Tang, W. Yang, Y. Du, D. Su, Y. Tan, S. Guo, *Adv. Mater.* (2018) e1807226.
- [14] W. Feng, L. Zhang, Y. Zhang, Y. Yang, Z. Fang, B. Wang, S. Zhang, P. Liu, *J. Mater. Chem. A* 5 (2017) 10311–10320.
- [15] L. Zhang, H. Zhang, B. Wang, X. Huang, F. Gao, Y. Zhao, S. Weng, P. Liu, *J. Mater. Chem. A* 7 (2019) 1076–1082.
- [16] H. Li, W. Tu, Y. Zhou, Z. Zou, *Adv. Sci.* 3 (2016) 1500389.
- [17] J. Jin, J. Yu, D. Guo, C. Cui, W. Ho, *Small* 11 (2015) 5262–5271.
- [18] Q.L. Xu, L.Y. Zhang, J.G. Yu, S. Wageh, A.A. Al-Ghamdi, M. Jaroniec, *Mater. Today* 21 (2018) 1042–1063.
- [19] F.Q. Zhou, J.C. Fan, Q.J. Xu, Y.L. Min, *Appl. Catal. B Environ.* 201 (2017) 77–83.
- [20] P. Zhou, J. Yu, M. Jaroniec, *Adv. Mater.* 26 (2014) 4920–4935.
- [21] L. Jiang, X. Yuan, G. Zeng, J. Liang, Z. Wu, H. Wang, *Environ. Sci. Nano* 5 (2018) 599–615.
- [22] A. Iwase, S. Yoshino, T. Takayama, Y.H. Ng, R. Amal, A. Kudo, *J. Am. Chem. Soc.* 138 (2016) 10260–10264.
- [23] H. Li, Y. Gao, Y. Zhou, F. Fan, Q. Han, Q. Xu, X. Wang, M. Xiao, C. Li, Z. Zou, *Nano Lett.* 16 (2016) 5547–5552.
- [24] L. Zhang, W. Feng, B. Wang, K. Wang, F. Gao, Y. Zhao, P. Liu, *Appl. Catal. B Environ.* 212 (2017) 80–88.
- [25] H. Li, Y. Sun, B. Cai, S. Gan, D. Han, L. Niu, T. Wu, *Appl. Catal. B Environ.* 170–171 (2015) 206–214.
- [26] Y. Min, G. He, Q. Xu, Y. Chen, *J. Mater. Chem. A* 2 (2014) 2578.
- [27] Y. Yang, Y. Zhang, Z. Fang, L. Zhang, Z. Zheng, Z. Wang, W. Feng, S. Weng, S. Zhang, P. Liu, *ACS Appl. Mater. Interfaces* 9 (2017) 6950–6958.
- [28] Z. Fang, S. Weng, X. Ye, W. Feng, Z. Zheng, M. Lu, S. Lin, X. Fu, P. Liu, *ACS Appl. Mater. Interfaces* 7 (2015) 13915–13924.
- [29] B. Wang, S. He, L. Zhang, X. Huang, F. Gao, W. Feng, P. Liu, *Appl. Catal. B Environ.* 243 (2019) 229–235.
- [30] Y. Wang, X. Huang, K. Wang, L. Zhang, B. Wang, Z. Fang, Y. Zhao, F. Gao, P. Liu, W. Feng, *J. Mater. Chem. A* 6 (2018) 9200–9208.
- [31] F. Gao, Y. Zhao, L. Zhang, B. Wang, Y. Wang, X. Huang, K. Wang, W. Feng, P. Liu, *J. Mater. Chem. A* 6 (2018) 18979–18986.
- [32] L. Zhang, J. Yuan, C. Jiang, X. Huang, Y. Zhao, F. Gao, Z. Fang, P. Liu, *Nanoscale* 11 (2019) 7825–7832.
- [33] S. Wang, B.Y. Guan, L. Yu, X.W.D. Lou, *Adv. Mater.* 29 (2017).
- [34] Y. Zeng, N. Guo, H. Li, Q. Wang, X. Xu, Y. Yu, X. Han, H. Yu, *Chem. Commun.* 55 (2019) 683–686.